Laser-induced Ultrasound Detection and Ranging (LuDAR) for 3D Imaging in Turbid Water

Jin Haoran
0022007@zju.edu.cn

⊠⊠⊠⊠

Geman Wu
Zhejiang University

Bokun Fang
Zhejiang University

Yike Zeng
Zhejiang University

Xu Gu
Zhejiang University

Xinzhi Ma
Zhejiang University

Zesheng Zheng
Agency for Science, Technology and Research (A*STAR)

Yuanjin Zheng
Nanyang Technological University

Keji Yang
Zhejiang University

Deqing Mei
Zhejiang University

Article

Keywords:

Posted Date: June 9th, 2026

DOI: https://doi.org/10.21203/rs.3.rs-9867686/v1

Additional Declarations: There is **NO** Competing Interest.

Laser-induced Ultrasound Detection and Ranging (LuDAR) for 3D Imaging in Turbid Water

Geman Wu[1,4], Bokun Fang[1,4], Yike Zeng[1,4], Xu Gu[1,4], Xinzhi Ma[1,4], Zesheng Zheng[5], Yuanjin Zheng[6], Keji Yang[1], Deqing Mei[1,2,3,4]*, Haoran Jin[1,3,4]*

[1]State Key Laboratory of Fluid Power and Mechatronic Systems, School of Mechanical Engineering, Zhejiang University, Hangzhou, China
[2]State Key Laboratory of Ocean Sensing, ZJU-Hangzhou Global Scientific and Technological Innovation Center, Zhejiang University, Hangzhou, China
[3]Institute of Fundamental and Transdisciplinary Research, Zhejiang University, Hangzhou, China
[4]Zhejiang Key Laboratory of Advanced Equipment Manufacturing and Measurement Technology, School of Mechanical Engineering, Zhejiang University, Hangzhou, China
[5]A*STAR Skin Research Labs (A*STAR SRL), Agency for Science, Technology and Research (A*STAR), Singapore
[6]School of Electrical and Electronic Engineering, Nanyang Technological University, Singapore
*Correspondence to:
Deqing Mei (medqmei@zju.edu.cn) or Haoran Jin (jinhr@zju.edu.cn)

Abstract

Underwater optical imaging is fundamentally constrained by optical scattering in turbid water. Although polarization imaging, time-gated imaging, and LiDAR can improve performance in turbid water, their reliance on optical detection leaves them inherently vulnerable to scattering-induced degradation. To address this limitation, a novel modality termed laser-induced ultrasound detection and ranging (LuDAR) for turbid-water 3D imaging is proposed. In LuDAR, laser-induced ultrasound is employed to encode optical absorption information into ultrasound waves, thereby circumventing optical scattering during detection. By rapidly scanning a pulsed laser beam in a LiDAR-like manner and detecting the ultrasound generated at each excitation point, high-fidelity 3D point clouds of the target are obtained. LuDAR was experimentally shown to remain effective at turbidity levels approximately twice those at which the representative optical methods became strongly degraded, while maintaining lateral resolution below 200 μm. The method uniquely combines optical-grade lateral resolution, low-scattering ultrasound propagation, and absorption-based 3D imaging, making it promising for turbid-water applications including underwater archaeology, infrastructure inspection, and marine resource exploration.

Introduction

Underwater optical imaging plays a central role in marine engineering inspection[1], ocean resource exploration[2], and underwater archaeology[3] owing to its high spatial resolution, intuitive visualization, and rich information. These advantages, however, rely on clear water with high optical transparency. In turbid environments, optical image quality deteriorates rapidly due to strong optical scattering. Acoustic techniques such as sonar thus dominate imaging in turbid conditions[4-6]. Nonetheless, underwater acoustic imaging suffers from inherent limitations: its spatial resolution is typically at a centimeter or even meter scale, and it captures only the structural outlines while lacking surface color or brightness information. In many high-precision inspection scenarios, acoustic imaging alone cannot replace the essential role of optical imaging[7]. Achieving high-quality optical imaging in turbid water therefore remains an important research topic and longstanding challenge.

In turbid water, suspended particles scatter light, producing both forward and backward scattering[8-11]. Forward scattering deviates photons from their original paths, leading to image blurring and reduced spatial resolution. Backward scattering, in contrast, redirects photons toward the detector, producing strong background noise and rapidly degrading the signal-to-noise ratio (SNR). In severe cases, the target information could even be completely overwhelmed by backward scattering noise, leading to optical imaging failure. To mitigate these effects, various strategies have been developed. Polarization imaging discriminates polarization-preserving target reflections from depolarized multiply scattered photons to suppress scattering noise[12-16]. Range-gated imaging synchronizes pulsed laser illumination with high-speed optical shutters to selectively capture target reflections within narrow temporal windows, rejecting a large portion of backscattered photons[17-19]. Light detection and ranging (LiDAR) scans the scene point-by-point with narrow laser beams, minimizing the illuminated area and thus reducing backscattered noise[20-26]. The spatial information of the target is retrieved from either photon time-of-flight (TOF) or geometric triangulation, enabling 3D point-cloud reconstruction. Metasurface-based pre-processing physically filters scattered light in the Fourier domain before detection, providing a hardware-level solution for imaging through turbid media[27,28]. Additionally, post-processing methods, such as deep learning, have been explored to recover degraded images by introducing prior knowledge or scattering physical models[29-35]. Although these methods improve optical imaging performance in turbid environments, they are fundamentally dependent on photons as the information carrier. As a result, these methods can only mitigate, but not completely eliminate, the effects of optical scattering. As turbidity increases, multiple scattering inevitably leads to severe SNR loss and resolution degradation.

In this paper, a novel three-dimensional imaging modality for turbid water environments, laser-induced ultrasound detection and ranging (LuDAR), is proposed. Specifically, LuDAR scans a pulsed laser beam across the target surface point by point in a LiDAR-like raster pattern. Through the laser-induced ultrasound effect, which shares the same thermoelastic generation mechanism widely exploited in biomedical optoacoustics[36-38], the spatial information of the target surface is encoded into ultrasound waves, which propagate robustly in turbid water. These ultrasound waves are then detected by ultrasonic transducers for imaging. As the information is carried via ultrasound waves rather than photons, the distortion from forward scattering of the reflected light is avoided. Moreover, ultrasonic transducers are insensitive to photons and thus inherently immune to optical backward scattering noise. Importantly, although LuDAR uses ultrasound as the information carrier, both image contrast and lateral spatial information remain optically encoded, thereby retaining optical contrast as an imaging signature. It can provide high-resolution 3D information similar to LiDAR, while capturing fine optical absorption-contrast features on the target surface, retaining the key advantages of optical imaging in turbid environments. By extending the turbidity tolerance of underwater optical imaging, LuDAR opens new avenues for high-precision marine inspection and exploration in challenging environments.

Results

LuDAR principle

As illustrated in Fig. 1a, LuDAR employs a point-scanning scheme analogous to LiDAR. A pulsed laser beam, directed by a beam deflector, illuminates discrete locations on the surface of the target immersed in turbid water with a high-resolution spot. Owing to the sufficiently short laser pulse duration, the absorbed energy is confined within the excitation volume. This leads to instantaneous heating and rapid thermoelastic expansion, generating a localized broadband ultrasound source at the excitation site[36-38] as illustrated in Fig. 1b. This laser-induced ultrasound (LU) propagates through the surrounding water as spherical waves. Unlike photons, which undergo strong multiple scattering in turbid media[39], LU has a wavelength larger than the size of suspended particles, allowing it to propagate through turbid water with minimal scattering (Fig. 1c). The LU waves from the excitation point are then detected by ultrasonic transducers. The recorded signals are subsequently processed using a synthetic aperture reconstruction algorithm to determine the corresponding 3D position of LU source. By raster-scanning the excitation beam across the field of view (FOV), a 3D point cloud representing the target surface is ultimately obtained. LuDAR combines optical-grade lateral resolution with ultrasound-based axial ranging accuracy. Exploiting robust ultrasound propagation and detection, it enables effective imaging at turbidity levels beyond those at which the conventional optical methods fail, while providing 3D imaging with unique optical absorption contrast in turbid underwater environments.

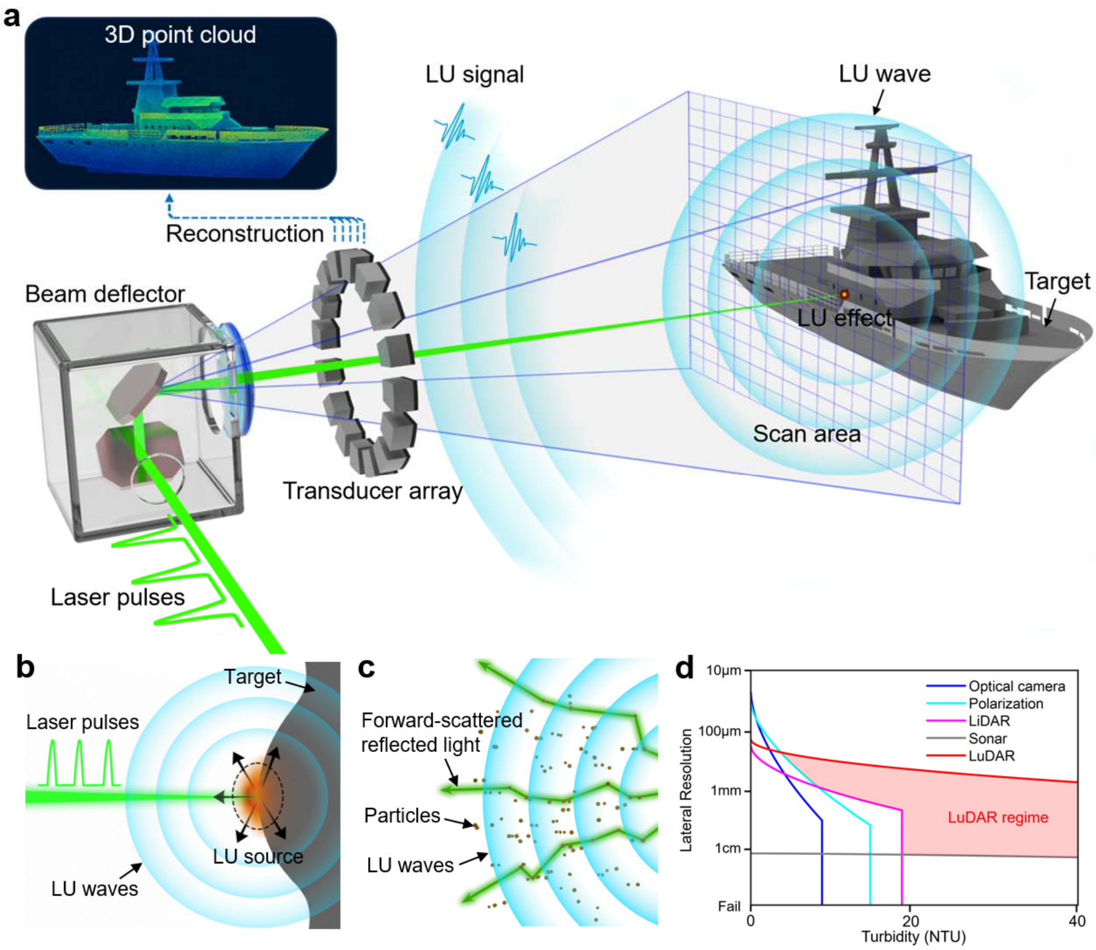

Figure 1 | Principle and performance of LuDAR. a, Schematic of the LuDAR imaging process. A pulsed laser beam is scanned across the target, generating a localized laser-induced ultrasound (LU) source at each excitation point. The resulting LU waves are detected by a transducer array and processed to reconstruct a 3D point cloud of the target surface. **b,** Mechanism of LU generation. Each short laser pulse leads to localized heating and rapid thermoelastic expansion, launching a broadband LU wave. **c,** Comparison of signal transmission in turbid water. Multiply scattered photons lose spatial information, whereas the longer-wavelength ultrasound preserves spatial information fidelity by propagating with negligible scattering. **d,** Conceptual comparison of lateral resolution versus turbidity at a working distance of 50 cm. Conventional optical methods degrade rapidly at low-to-moderate turbidity, while sonar remains operational but resolution-limited. LuDAR occupies the upper-right domain, maintaining hundred-micrometer resolution well into the high-turbidity regime (shaded red).

Fig. 1d provides a conceptual comparison of representative modality trade-offs at a 50 cm working distance. Conventional camera imaging offers the highest resolution in clear water (tens of micrometers), but degrades rapidly with increasing turbidity. The favorable imaging performance of polarization imaging can only be maintained up to approximately 15 NTU. LiDAR starts with lower resolution but degrades more gradually, persisting into about 20 NTU before failing. Sonar operates across a broad turbidity range but its resolution remains low, on the centimeter scale. LuDAR distinctly occupies the upper-right domain of this parameter space: it maintains lateral resolution of about one hundred micrometers, while exhibits the slowest degradation with increasing turbidity among all optical methods. Notably, conventional optical modalities fail in water with turbidity beyond 20 NTU, whereas LuDAR remains effective well into higher-turbidity regimes. The shaded red region marks the exclusive domain where LuDAR bridges the gap between turbidity-intolerant optics and coarse-grained sonar. Other functional comparison of different imaging modalities is provided in Supplementary Table S1.

System implementation, calibration and reconstruction framework

A LuDAR system framework is illustrated in Fig. 2a, comprising a pulsed laser, an optical module, a scanning module, an ultrasonic transducer array, a data acquisition (DAQ) module, and an integrated controller with signal processor. A nanosecond pulsed laser is employed to excite LU waves with millimeter-scale wavelengths that propagate effectively through turbid water. The optical module delivers the beam into the scanning module, which deflects the beam to perform a 2D raster scan across the target surface. Upon entering the water, the beam impinges on the target surface and generates a localized LU source. The resulting LU waves are captured by a multi-element transducer array, which expands the effective receiving aperture and enhances signal quality, and are digitized by the DAQ module. A photodetector is used to synchronize excitation and acquisition. The integrated controller advances the scanning module to the next position after each acquisition is completed. The detailed setup is provided in the Methods section. Following the hardware deployment of LuDAR, system calibration and image reconstruction methods are required.

To achieve accurate 3D reconstruction, both the optical ray trajectories in water and the spatial pose of the transducer array should be characterized. Owing to beam refraction by the air-glass-water interface, the mapping between galvanometer deflection and the incident ray trajectories in water is unknown a priori. As schematically illustrated in Fig. 2b, the ray trajectory for each deflection was determined by the laser spot at two planes of different depths. The mapping was then established through angle-by-angle scanning (see Methods for details). With the optical ray trajectories determined, the spatial pose of each transducer was subsequently calibrated using the LU signals acquired from a set of scan points with known 3D coordinates (Fig. 2c). The distances from these scan points to each transducer, derived from the TOF of the corresponding LU signals, were combined to determine the 3D position of the transducer via a nonlinear least-squares fit. Concurrently, the orientation of each transducer was taken as the direction from its fitted position to the scan point that yielded the maximum LU amplitude. Calibration results are provided in Supplementary Section S3.

Based on the calibrated system, 3D surface reconstruction of the target was performed using a ray-constrained weighted delay-and-sum (RC-WDAS) algorithm tailored for LuDAR. As illustrated in Fig. 2d, the calibrated optical ray for each scan position confines the LU source to a one-dimensional line. Candidate source points along the ray were scored by weighted summation of the corresponding envelope amplitudes from all transducers, with weights derived from an approximate transducer sensitivity model based on the receiver directivity (see Supplementary Section S4). The point yielding the maximum synthesized intensity was taken as the surface location. Repeating this procedure across the raster scan produced a 3D point cloud of the target surface (Fig. 2e). Implementation details are provided in the Methods section.

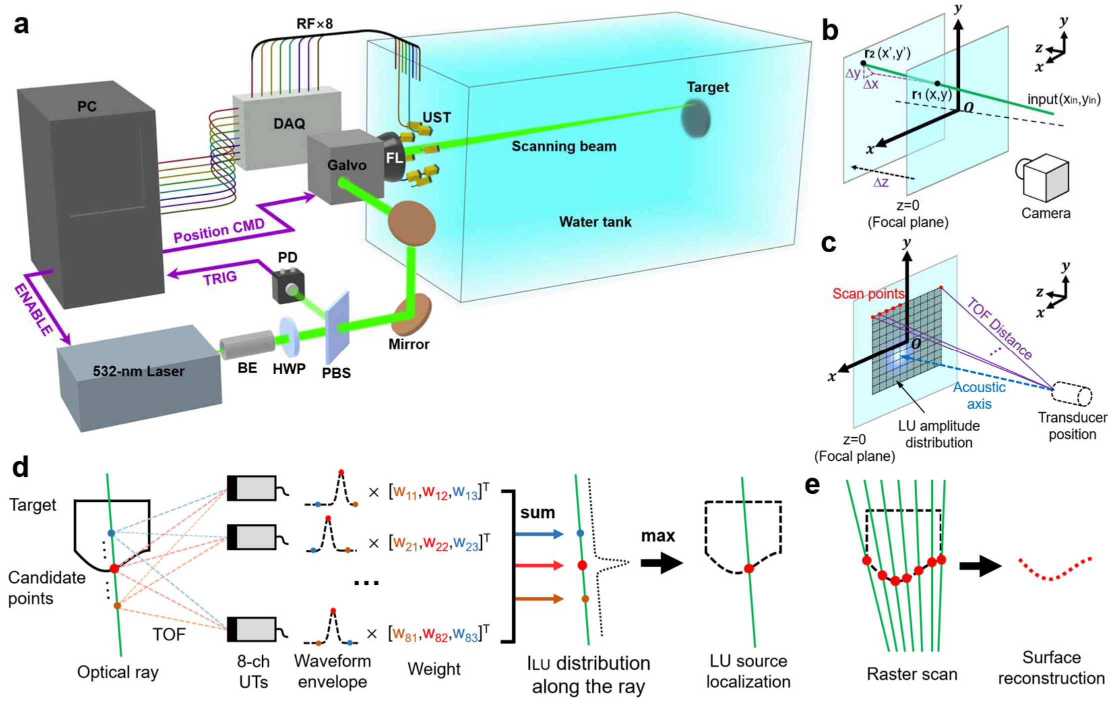

Figure 2 | LuDAR system implementation, calibration, and reconstruction. a, System architecture. BE: beam expander; HWP: half-wave plate; PBS: polarizing beam splitter; PD: photodetector; Galvo: galvanometer; FL: field lens; UST: ultrasonic transducer array; RF×8: eight-channel radio-frequency signals; PC: personal computer for integrated control and signal processing. The optical module encompasses the BE, HWP, PBS and mirrors; the scanning module includes the Galvo and FL. **b,** Schematic of the experimental ray calibration procedure: laser-spot coordinates are recorded at two depths to determine the ray trajectory for each galvanometer input. **c,** Transducer array pose calibration, showing the multilateration approach for position recovery and the determination of the acoustic axis toward the point of maximum LU amplitude. **d,** RC-WDAS principle: the LU source is confined to a calibrated ray, and the surface point is identified by weighted summation of multichannel ultrasonic signals. **e,** Reconstructed 3D point cloud of an example target.

Resolution robustness under increasing turbidity

The lateral resolution of LuDAR was quantified under increasing turbidity with edge-spread analysis. The laser spot was scanned across a knife edge (see Methods), and the signals from all transducer channels were synthesized via the RC-WDAS algorithm, yielding a one-dimensional intensity profile across the edge. This amplitude profile was fitted to derive the edge spread function (ESF). The line spread function (LSF) was then obtained by differentiating the

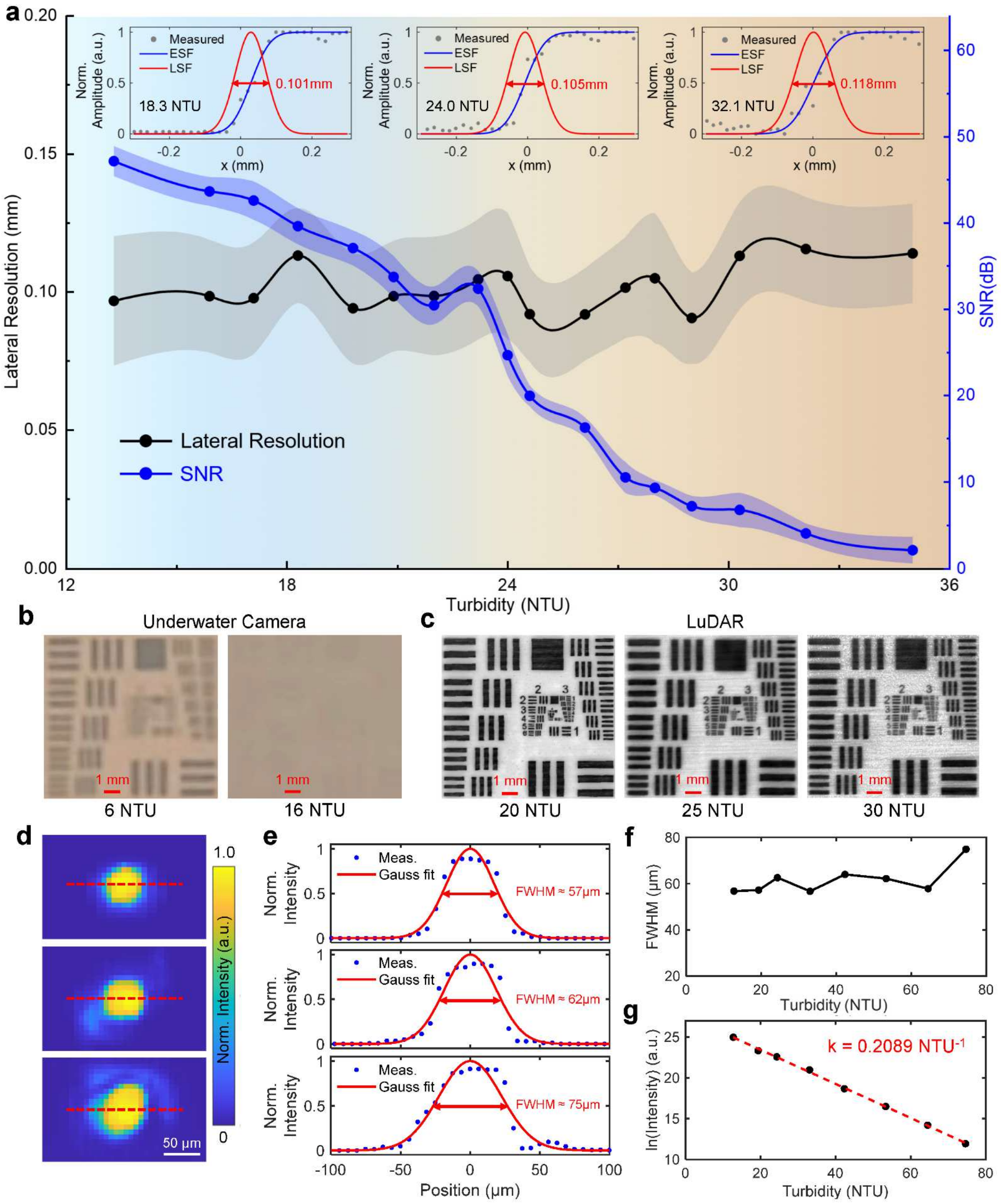

Figure 3 | Resolution robustness and beam stability under increasing turbidity. **a, Top:** representative edge-spread function (ESF) and line-spread function (LSF) curves at three turbidity levels, with the corresponding lateral resolution (FWHM) annotated. **Bottom:** mean lateral resolution (black, left y-axis) and SNR (blue, right y-axis) as functions of turbidity. Error bars indicate ±1 standard deviation over 100 repeated scans. **b,** Underwater optical camera images of a USAF 1951 resolution target acquired at a working distance of 50 cm, which became indiscernible by 16 NTU. **c,** LuDAR amplitude-encoded front views acquired at the same working distance with a scanning step of 50 μm, preserving target details at higher turbidities. **d,** Focal-spot intensity distributions recorded at 24, 53, and 74 NTU. **e,** Lateral intensity profiles (points) extracted from the spots in **d**, fitted with Gaussian functions (solid lines). **f,** Spot width (FWHM) versus turbidity, showing only minor broadening across the tested range. **g,** Attenuation of the maximum focal intensity (log scale) with increasing turbidity. The linear fit indicates an exponential decay, consistent with the Lambert-Beer law.

ESF, and its full width at half maximum (FWHM) was taken as the measure of lateral resolution. Representative ESF and LSF curves from a single acquisition at turbidities of 18.3, 24.0, and 32.1 NTU are shown in Fig. 3a (top panels), with corresponding lateral resolutions measured as 0.101 mm, 0.105 mm, and 0.118 mm, respectively. The black curve in Fig. 3a (left y-axis) shows the mean lateral resolution at each turbidity, with error bars indicating the standard deviation over 100 repeated edge scans. The resolution exhibited no significant degradation across the tested turbidity range, demonstrating the robustness of LuDAR to turbidity-induced resolution degradation. The SNR evaluated from the same edge-scan data (see Methods) is shown by the blue curve in Fig. 3a (right y-axis). For comparison, Fig. 3b presents images of a standard USAF 1951 resolution target (see Supplementary Section S5) acquired with an underwater optical camera at a working distance of 50 cm. As turbidity increased, optical visibility deteriorated rapidly; the target had become completely indistinguishable from the background by 16 NTU. LuDAR images acquired at the same working distance under higher turbidity levels are also shown (Fig. 3c), with a scanning step of 50 μm to ensure adequate spatial sampling. Compared with the underwater camera, LuDAR exhibited substantially greater turbidity tolerance, maintaining high imaging fidelity even in highly turbid conditions. At 30 NTU, the reconstructed LuDAR image resolved Group 2, Element 2 of the USAF 1951 target, corresponding to a lateral resolution of 111.36 μm according to the target lookup, consistent with the knife-edge measurements.

To assess focal spot broadening from forward scattering under increasing turbidity, the optical intensity distribution at the focal plane was directly recorded using a beam profiler (see Methods). Appropriate combinations of neutral-density filters were used to prevent sensor saturation at each turbidity level. Representative focal spot images acquired at turbidities of 24, 53, and 74 NTU are shown in Fig. 3d. For each image, the lateral optical intensity profile was extracted along the red dashed line, centered at the pixel of maximum intensity, and fitted with a Gaussian function, yielding FWHM values of 57 μm, 62 μm, and 75 μm, respectively (Fig. 3e). Across the full set of eight turbidity levels (12.7-74.6 NTU), the FWHM exhibited only a minor upward trend (Fig. 3f). Meanwhile, Fig. 3g shows the natural logarithm of the maximum optical intensity (after compensation for filter attenuation) as a function of turbidity. A linear fit indicates an exponential decay of intensity with increasing turbidity. The fitted slope corresponds to a turbidity attenuation coefficient $k = 0.2089$ NTU^{-1}, consistent with the Lambert-Beer law[40]. These results demonstrate that the excitation beam maintains robust spatial confinement under elevated turbidity, indicating that LuDAR has the potential to operate in even more turbid waters provided sufficient laser pulse energy is available.

Quantitative 3D surface reconstruction accuracy

To quantitatively evaluate the 3D imaging accuracy of LuDAR in turbid water, a 3D-printed dolphin model with a complex curved surface was employed as the target (Fig. 4). The reference point cloud was generated by sampling the visible surface of the original digital model from the LuDAR viewing direction, whereas the LuDAR point cloud was acquired in water with turbidity of 25 NTU. The corresponding depth-encoded point clouds are presented in Figs. 4a and 4b, respectively. Despite the intricate topology of the model surface, the reconstructed point cloud faithfully reproduced the key geometric features, including the dorsal fin and hollow structures, and exhibited a depth-encoded color distribution matching that of the reference.

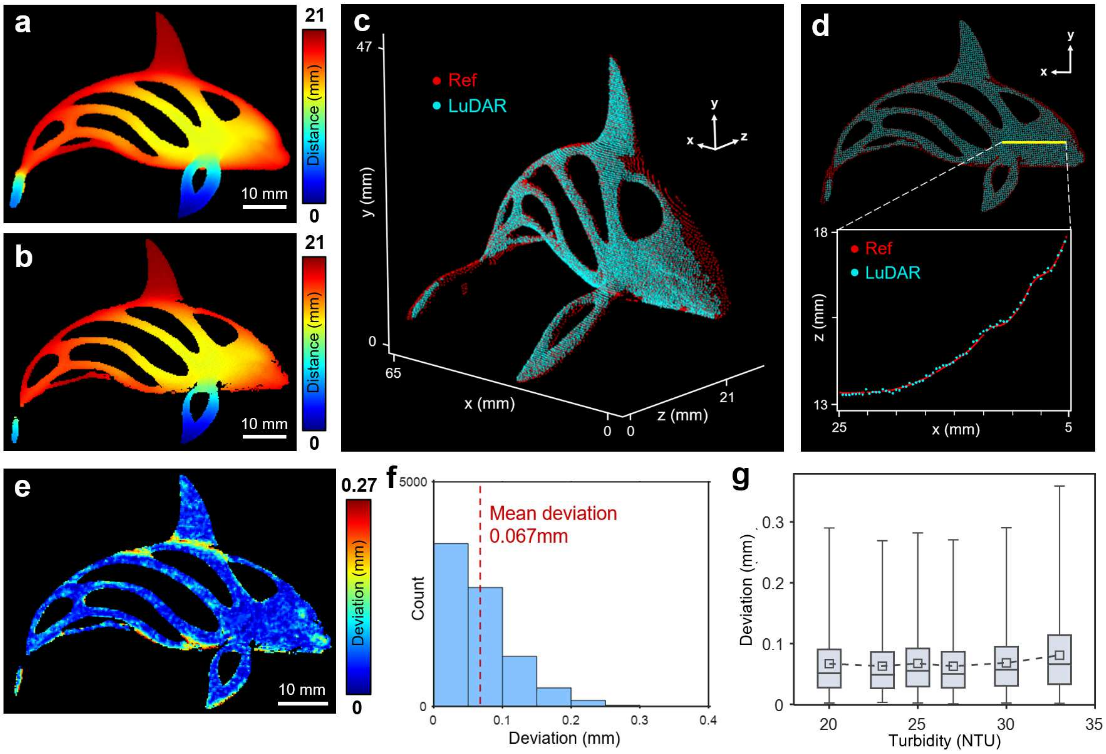

Figure 4 | Quantitative evaluation of 3D surface reconstruction accuracy using a dolphin model. a, Depth-encoded reference point cloud generated from the digital model. **b,** Depth-encoded LuDAR-reconstructed point cloud acquired at 25 NTU. **c,** Registration result after rigid ICP alignment, with reference (red) and measured (cyan) point clouds superimposed. **d,** Cross-sectional profiles extracted along the yellow line, showing close agreement between the reference and reconstructed surfaces. **e,** Deviation map of the registered reconstruction after outlier exclusion, colored by per-point deviation magnitude (Gaussian-smoothed for visual clarity; σ = 0.2 mm). **f,** Histogram of per-point deviations at 25 NTU, yielding a mean deviation of 0.067 mm. **g,** Box plots of per-point registration deviations at each turbidity level (boxes: interquartile range; central lines: median; squares: mean; dashed line: mean trend). The median and mean deviations remain nearly constant up to 30 NTU.

The measured point cloud was first registered to the reference point cloud for accuracy evaluation. Rigid registration was performed using the iterative closest point (ICP) algorithm (see Methods), in which a global rigid transformation, comprising rotation and translation, was iteratively optimized to minimize the root-mean-square (RMS) of the registration deviations. Fig. 4c displays the registered result, with red and cyan points denoting the reference and LuDAR point clouds, respectively. A representative cross-sectional profile was extracted from both point clouds along the yellow line indicated in Fig. 4d. The two profiles exhibit close agreement and nearly overlap, with only small local deviations of the reconstructed surface from the reference. The spatial distribution of deviations is further illustrated by the map in Fig. 4e, which reveals a largely uniform deviation distribution. Slightly larger deviations observed at a few isolated locations are attributed to printing-related deformation of the physical model and residual reconstruction error. The statistical distribution of deviations at 25 NTU is summarized in the histogram of Fig. 4f, yielding a mean deviation of 0.067 mm. Measurements were repeated at 20, 23, 27, 30, and 33 NTU. Fig. 4g presents box plots of the registration deviations at each turbidity level. The median and mean errors remain nearly constant up to 30 NTU and show a slight increase at 33 NTU, due to reduced LU signal amplitudes, which introduced spurious points into the reconstructed point cloud and compromised registration accuracy. Full histograms are available in Supplementary Section S6.

Comparison with representative underwater optical imaging modalities

To compare LuDAR against representative optical approaches for underwater imaging, a circular stainless-steel emblem featuring raised logos, text, and a surface relief height of approximately 2-4 mm was imaged using three optical modalities: direct camera imaging, polarization-based imaging, and triangulation-based LiDAR. The resulting images were then compared with those obtained by LuDAR. Figures 5a-d display the reconstructed images of each modality at turbidities of 8, 14, and 18 NTU, with LuDAR additionally evaluated at 36 NTU. For LiDAR and LuDAR, the 3D point clouds are rendered with height-encoding.

Under 18 NTU, camera imaging failed completely, revealing no discernible structural features of the emblem (Fig. 5a). Polarization-based imaging revealed only a blurred circular outline and a blurred central emblem motif, with the surrounding text details remaining unresolved (Fig. 5b). LiDAR exhibited substantial point dropout and indistinct geometric delineation, indicating that the technique was approaching its operational limit at this turbidity since the backscattered background noise had nearly overwhelmed the laser spot (Fig. 5c). In particular, specular regions such as the central motif resulted in large blind areas where most of the reflected light was directed away from the receiver. In contrast, LuDAR faithfully reconstructed the fine surface structures of the emblem at 18 NTU, and maintained clearly recognizable reconstructions even at 36 NTU (Fig. 5d), demonstrating turbidity tolerance far exceeding that of the other three modalities.

To enable a quantitative comparison across both 2D and 3D modalities, the structural edges of the emblem were extracted from each image or height map and compared against a binary edge reference derived from the CAD model (see Methods). The precision and recall of the extracted edges were evaluated,

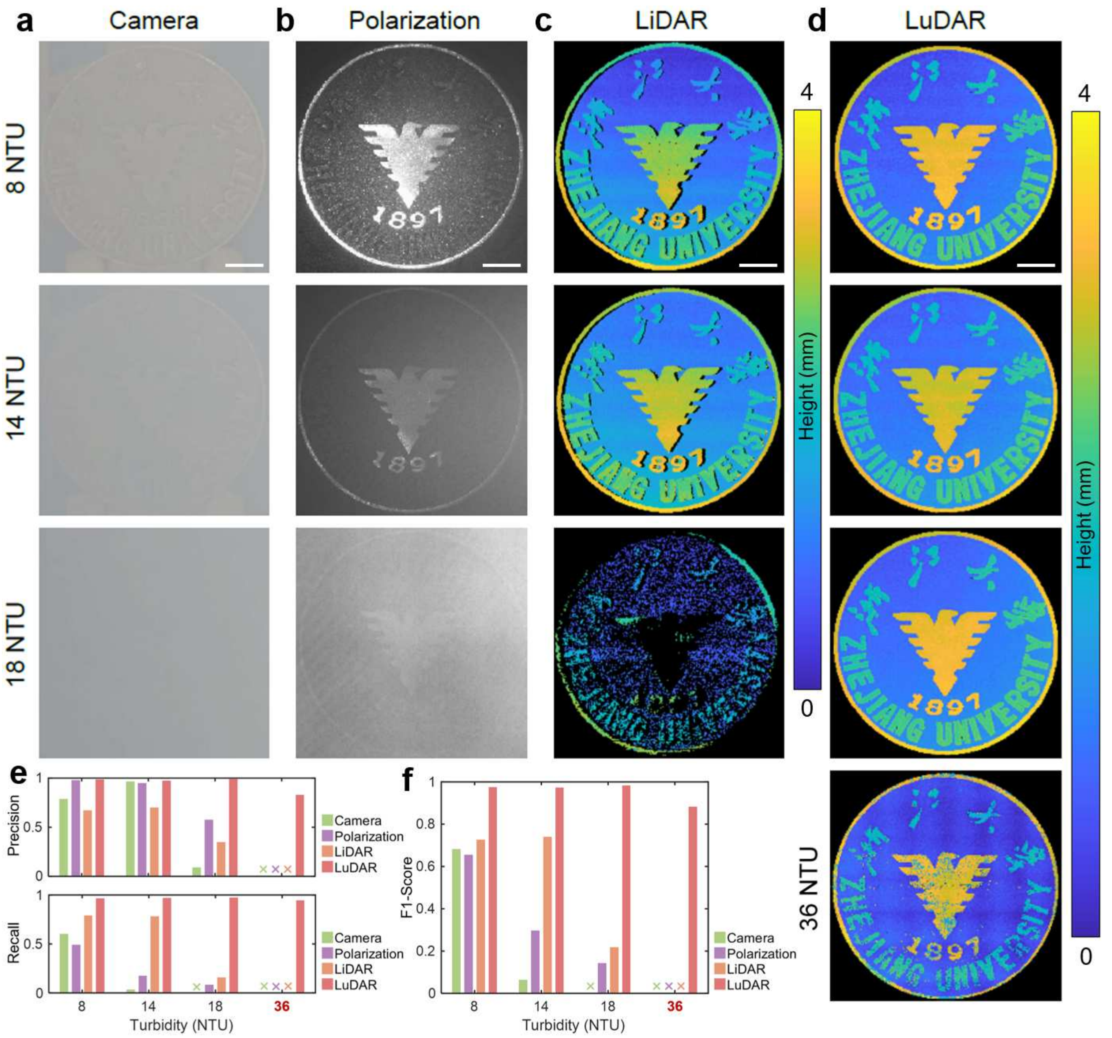

Figure 5 | Comparative imaging of a stainless-steel emblem under increasing turbidity. a, Direct camera images at 8, 14, and 18 NTU, showing complete failure at 18 NTU. **b,** Polarization-difference images at the same turbidities, recovering only a blurred circular outline and the central motif at 18 NTU. **c,** Triangulation-based LiDAR height-encoded reconstructions at the same turbidities, exhibiting substantial point dropout and large blind areas in specular regions at 18 NTU. **d,** LuDAR height-encoded reconstructions at 8, 14, 18, and 36 NTU, faithfully resolving fine surface structures across all tested turbidities and remaining clearly recognizable even at 36 NTU. **e,** Precision (P) and recall (R) bar charts at the tested turbidities for all four methods, evaluated against a CAD-derived binary edge reference. **f,** Corresponding F1-scores. Scale bars in **a-d**, 10 mm.

where precision measures the fraction of extracted edges that are true, and recall measures the fraction of reference edges correctly recovered. Figure 5e presents the precision (P) and recall (R) as bar charts at the tested turbidities for all four methods, and the corresponding F1-scores are shown in Fig. 5f.

Camera imaging suffered the fastest F1-score decline, while polarization-based imaging degraded more gradually. The low recall of polarization-based imaging is largely attributed to the poor recovery of the non-specular surrounding text, which tends to depolarize the reflected light and become indistinguishable from the background after polarization filtering.

LiDAR maintained a relatively good F1-score at 8 and 14 NTU but suffered a sharp drop at 18 NTU. In contrast, LuDAR consistently achieved the highest recall and precision among all modalities. Up to 18 NTU, its recall remained above 0.96 and precision above 0.97, yielding F1-scores exceeding 0.97. At 36 NTU, LuDAR still maintained an F1-score of 0.74. These quantitative results confirm that LuDAR uniquely combines high turbidity tolerance with accurate geometric recovery, extending the effective operating range well beyond that of representative underwater optical methods.

High-fidelity imaging of the complex ship model in turbid water

To further demonstrate the capability of LuDAR for high-fidelity 3D imaging of complex targets in turbid water, a detailed metallic ship model was imaged at 25 NTU and a working distance of 50 cm. The model (approximately 145 × 120 × 45 mm) incorporates rich fine-scale features, including multiple masts, rigging, perforated sails, and deck structures (Supplementary Section S7). A scanning step of 0.25 mm was employed, yielding approximately 300,000 scan positions.

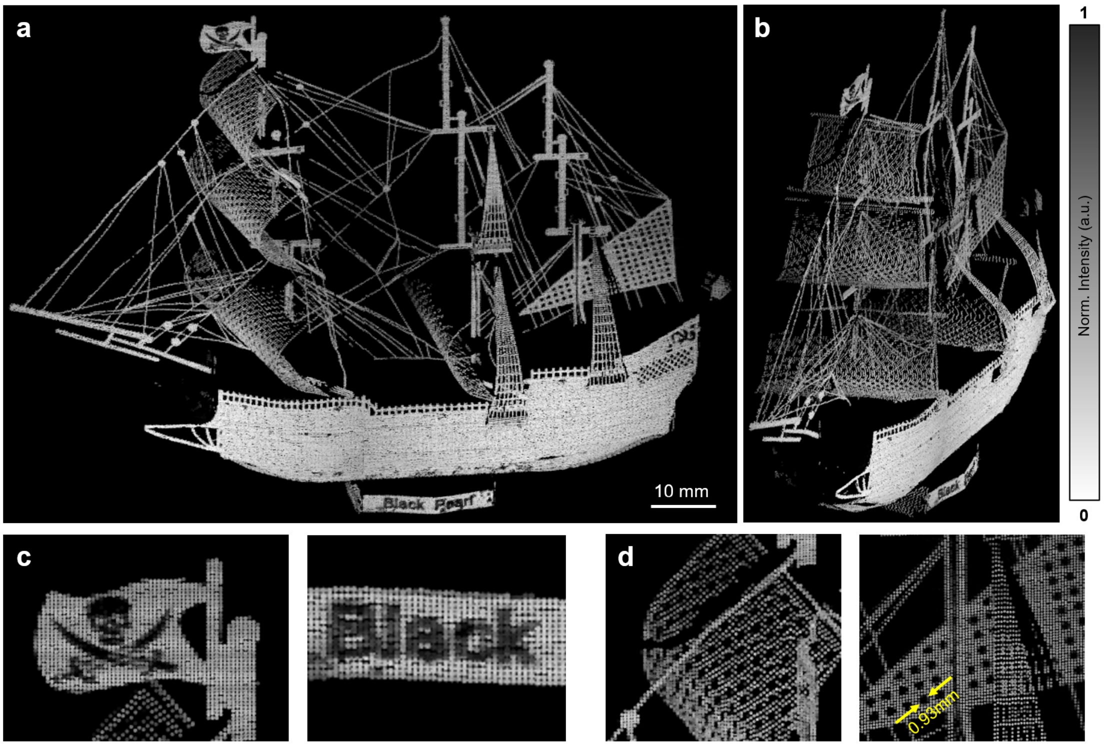

Figure 6 | High-fidelity 3D reconstruction of a complex ship model at 25 NTU and a working distance of 50 cm. a,b, Oblique top and side views of the LuDAR point cloud, rendered with grayscale LU amplitude encoding, faithfully reproducing fine structural details across the vessel. **c,** Magnified view of the sail flag and base region, where the skull emblem and lettering are clearly resolved by optical absorption contrast. **d,** Magnified view of the perforated sails. The hole indicated by the yellow arrow measures 0.93 mm in diameter, closely matching the true dimension of 1 mm.

Fig. 6a-b display oblique top and side views of the reconstructed point cloud, respectively, rendered with grayscale LU amplitude encoding. The reconstruction accurately captures the overall morphology of the vessel while faithfully resolving fine structural details, such as the deck railings, the masts and spars with connecting rigging, and the perforated sailcloth. Magnified views of selected regions in Fig. 6a are provided in Figs. 6c and 6d. In Fig. 6c, the skull emblem on the sail flag and the lettering on the base are clearly distinguished by amplitude contrast, demonstrating the ability of LuDAR to capture optical contrast information in addition to geometry. Fig. 6d focuses on the perforated sails, where the hole indicated by the yellow arrow yields a measured diameter of 0.93 mm, closely matching the actual dimension of 1 mm. These results confirm that LuDAR enables high-fidelity 3D reconstruction of complex, multi-scale objects in turbid water, while recovering optical absorption-based contrast features beyond geometry. This capability highlights the potential of LuDAR for practical underwater inspection and exploration tasks.

Discussion

In this work, a novel underwater 3D imaging modality, termed laser-induced ultrasound detection and ranging (LuDAR), is proposed to address the long-standing challenge of optical scattering in turbid underwater imaging. By encoding target surface optical absorption into ultrasound waves and detecting them with a multi-element transducer array, LuDAR circumvents the optical scattering that fundamentally limits existing optical methods. A proof-of-concept system was built and experimentally shown to provide a turbidity tolerance approximately twice that of representative optical methods at a working distance of 50 cm, with lateral resolution remaining below 200 μm. Quantitative validation on a complex dolphin model yielded a mean surface deviation of 0.067 mm at 25 NTU, while high-fidelity imaging of a metallic ship model at the same turbidity demonstrated the capability of LuDAR for complex target perception. These capabilities position LuDAR as a promising tool for demanding underwater tasks including high-precision archaeological documentation, infrastructure inspection, and offshore asset monitoring.

The practical performance envelope of LuDAR has not yet been fully explored. Higher scanning efficiency may be achieved by replacing the present galvanometer-based raster scan with agile beam-steering architectures, such as chip-scale acousto-optic deflectors, MEMS or silicon-photonic focal-plane switch arrays, and metasurface-assisted scanners[41-43]. Moreover, selecting lasers with higher pulse energy can further enhance turbidity resistance, and recent advances in high-brightness laser sources may enable more compact, energy-efficient excitation modules suitable for field deployment[44]. Notably, as an optical-absorption-based imaging modality, LuDAR provides information complementary to that of existing reflection-based optical imaging methods. This complementary information, when combined, enables more comprehensive underwater perception. On the hardware level, integration is further facilitated: the excitation laser source could be shared with LiDAR, and the ultrasonic transducer array is compatible with sonar architectures. These attributes position LuDAR as a promising next-generation imaging platform for turbid underwater environments.

Methods

LuDAR system setup

A schematic of the LuDAR system is provided in Fig. 2a. A pulsed laser (FORMULA-532-D, Inno Laser) with a wavelength of 532 nm, pulse width of 80 ns, pulse energy of approximately 3 mJ, and repetition rate of 2 kHz was employed as the optical source. The wavelength of 532 nm was selected for its low attenuation in water. The laser beam, with an initial diameter of approximately 1 mm, was expanded eightfold by a beam expander (E-532-8X, Inno Laser) to a diameter of approximately 8 mm and then passed through a half-wave plate (GWPLH532, Jinwei Scientific) and a polarizing beam splitter (HCBS2, Hengyang Optics). At the beam splitter, a small fraction of each pulse was directed onto a photodetector (PD50A, Xunmiao Optoelectronics), whose output was processed by a transimpedance amplifier (OPA847, KEYI Electronics) followed by a comparator module (TLV3501, KEYI Electronics) to generate a TTL trigger pulse for synchronized data acquisition. The main beam was steered by two dielectric high-reflection mirrors (HLM-532, Hengyang Optics) into a galvanometer scanner (L143-R, Ouya Laser) and subsequently focused by a field lens (FL-532, Ouya Laser, focal length f = 420 mm). The focused beam entered the water tank through a 5 mm thick glass window and impinged on the target surface, with a focal spot diameter below 100 μm throughout the investigated turbidity range (Fig. 3d-f). The working distance, defined as the optical path length from the inner surface of the glass window to the target, was set to 50 cm across all experiments. Optical absorption at the excitation site generated a localized laser-induced ultrasound (LU) source that radiated ultrasonic waves into the surrounding water. The LU waves were detected by an eight-element ultrasonic transducer array (WI-30C, Shantou Ultrasound) with a center frequency of 1 MHz and a −6 dB bandwidth ranging from 200 kHz to 2.5 MHz. The received signals were then amplified by low-noise preamplifiers (LNA, LOCKZHINER Electronics) with a gain of 46 dB and digitized by an eight-channel data acquisition card (PCIe8586M, ART Technology) operating at a sampling rate of 20 MHz. The acquired multichannel waveforms were subsequently processed using the RC-WDAS algorithm to reconstruct the 3D surface of the target.

System Calibration

To establish the mapping between the galvanometer input commands and optical ray trajectories in water, a direct experimental calibration was performed as illustrated in Fig. 2b. The galvanometer scanner took the intended focal-plane coordinates (x_{in}, y_{in}) as its input (corresponding to a certain deflection), with built-in correction ensuring accurate spot positioning (validated in

Supplementary Section S2). The ray trajectories corresponding to a set of different input commands were measured. A calibration grid was positioned at the focal plane (z = 0), and the laser-spot coordinates (x, y) were recorded for all input commands. The grid was then translated by Δz (specifically 10 mm) along the z-axis, and the laser-spot coordinates (x’,y’) were also recorded. For each command, the two recorded points $\mathbf{r_1}$ = (x, y, 0) = (x_{in}, y_{in}, 0) and $\mathbf{r_2}$ = (x', y', Δz) defined a unique optical ray, whose slope components were computed as m_x = (x'-x)/Δz and m_y = (y'-y)/Δz. The measured slope values across all tested commands were linearly interpolated to ultimately obtain a mapping from input coordinates (x_{in}, y_{in}) to the ray slopes (m_x, m_y) (see Supplementary Section S2). For any given input (x_{in}, y_{in}), the corresponding optical ray is uniquely defined by the point $\mathbf{r_1}$ = (x_{in}, y_{in}, 0) and the direction vector (m_x, m_y, 1).

The spatial pose of each transducer was subsequently calibrated (Fig. 2c). An aluminum plate positioned at the focal plane was raster-scanned in the x-y plane over a 30 × 30 point grid with a 2 mm spacing. For each transducer, the time-of-flight of the LU signal generated at each scan point was recorded and converted to a source-detector distance estimate. These distance estimates were then used to determine the 3D coordinates of each transducer via a nonlinear least-squares fitting procedure. From the same scan, the acoustic axis of each transducer was taken as the direction from its fitted position toward the scan point that yielded the maximum LU amplitude. Complete calibration results are provided in Supplementary Section S3.

RC-WDAS reconstruction

Three-dimensional surface reconstruction was performed using the RC-WDAS framework (Fig. 2d). For each laser scan position, the calibrated optical ray constrained the LU source to a one-dimensional line, collapsing the volumetric localization problem into a line search. Within a depth range of interest, each ray was discretized with a step size of 0.01 mm, generating a set of candidate points $\boldsymbol{r}$. For each candidate point $\boldsymbol{r}$, the ultrasound time of flight to the *i*-th transducer was computed as $t_i(\boldsymbol{r}) = \|\boldsymbol{r} - \boldsymbol{r_i}\|/c$, where $\boldsymbol{r_i}$ denotes the calibrated position of the *i*-th transducer and c is the speed of sound in water, taken as 1483 m/s for the experimental conditions. Simultaneously, the angle $\theta_i(\boldsymbol{r})$ between the vector $\boldsymbol{r} - \boldsymbol{r_i}$ and the calibrated acoustic axis of the *i*-th transducer was calculated.

The envelope amplitude $A_i(t_i(\boldsymbol{r}))$ of the Hilbert-transformed A-scan at the computed arrival time was obtained by linear interpolation. The weight function $w(\theta)$, determined by the transducer directivity (see Supplementary Section S4), was used to assign a weight to each channel based on the precomputed angle $\theta_i(\boldsymbol{r})$. The synthesized response at the candidate point was then evaluated as a normalized weighted sum over all transducer channels:

$$S(\boldsymbol{r}) = \frac{\sum_{i=1}^{N} w(\theta_i(\boldsymbol{r}))A_i(t_i(\boldsymbol{r}))}{\sum_{i=1}^{N} w(\theta_i(\boldsymbol{r}))} \tag{1}$$

where N denotes the total number of transducers. The denominator normalizes the weighted sum to avoid artificial amplitude differences introduced by variations in the total weight. The candidate point along the ray that yielded the maximum synthesized response $S(\boldsymbol{r})$ was selected as the estimated LU source location for that scan position. Repeating this procedure across all scan positions produced a 3D point cloud representation of the object surface.

Resolution characterization

Lateral resolution was evaluated using a knife edge placed at the 50 cm focal plane. The laser beam was scanned across the edge with a step size of 20 μm. At each scan position, 50 laser shots were averaged and the signals from all eight transducer channels were synthesized via the RC-WDAS algorithm. The resulting amplitude profile was fitted with an Error Function to obtain the ESF, from which the LSF was derived. The lateral resolution was defined as the full width at half maximum (FWHM) of the LSF. For statistical robustness, 100 repeated edge scans were performed at each turbidity level. The SNR of the reconstructed edge profile was evaluated from the same data as $\mathrm{SNR} = 20\log_{10}(A_{\mathrm{target}}/A_{\mathrm{background}})$, where A_{target} and $A_{\mathrm{background}}$ denote the mean envelope amplitudes of reconstructed points in the target region and background region, respectively. Specifically, the target region was defined as reconstructed points with lateral positions between 0.1 mm and 0.3 mm from the edge, whereas the background region was defined as points between −0.3 mm and −0.1 mm.

To assess practical imaging performance, a USAF 1951 resolution target (DaFan Optics) was imaged at the same working distance, with a scanning step of 50 μm covering a field of view of approximately 10 mm × 10 mm.

Focal-spot characterization was performed using a beam profiler (LH-360, Lianhuicheng Technology) with a pixel pitch of 6.25 μm, encapsulated in a transparent waterproof enclosure and submerged such that its sensing plane coincided with the focal plane. To prevent sensor saturation, neutral-density filters with nominal transmittances of 0.1%, 1%, 10%, and 50% were used in various combinations, yielding overall attenuation factors ranging from 1×10^{-8} to 5×10^{-3} for the different turbidity conditions investigated (12.7-74.6 NTU).

3D surface reconstruction accuracy evaluation

A 3D-printed dolphin model was placed on a transparent acrylic platform at a working distance of 50 cm. The reference point cloud was generated by densely sampling the original digital model of the dolphin. To avoid incorrect correspondences caused by overlapping internal structures in the model, a visibility-based filter was applied: sampling was performed along the same viewing direction as the LuDAR acquisition, retaining only the first surface intersected along each line of sight.

The reconstructed point cloud was preprocessed to remove background noise prior to accuracy evaluation. Points with LU amplitude below −6 dB relative to the maximum reconstructed amplitude were discarded. Subsequently, a k-nearest neighbor (KNN) outlier filter was applied to remove isolated points. After preprocessing, the reconstructed point cloud was registered to the reference point cloud using a point-to-point iterative closest point (ICP) algorithm. The rigid transformation (rotation and translation) was iteratively optimized to minimize the root-mean-square (RMS) nearest-neighbor distance between the reconstructed and reference point clouds until convergence. For each point in the reconstructed cloud, the deviation was defined as the Euclidean distance to its nearest neighbor in the reference cloud. Deviations lying outside the interval [Q1 − 3 × IQR, Q3 + 3 × IQR], where IQR denotes the interquartile range, were conservatively classified as outliers and excluded from subsequent deviation analysis. The outlier-filtered distributions were used to generate the deviation map (Fig. 4e), histogram (Fig. 4f), box plots (Fig. 4g), and Supplementary Fig. S6. The excluded fractions were 1.41%, 0.75%, 0.69%, 1.25%, 0.45%, and 1.13% at 20, 23, 25, 27, 30, and 33 NTU, respectively, remaining below 1.5% in all cases.

Comparative imaging experiments

A circular stainless-steel emblem (60 mm diameter, surface relief of 2-4 mm) was placed at a working distance of 50 cm. Conventional camera imaging, polarization imaging, and triangulation-based LiDAR were evaluated at turbidities of 8, 14, and 18 NTU, whereas LuDAR was additionally evaluated at 36 NTU.

For conventional camera imaging, an underwater camera (UW-S5-3PBX10, Barlus) was used to acquire direct images under active illumination from the camera's built-in light source.

Polarization-based imaging employed linearly polarized laser illumination at a wavelength of 532 nm, expanded by a plano-convex lens to cover the target with a beam diameter of approximately 80 mm. A polarization camera (MER2-502-79U3MPOL, Daheng Imaging) recorded intensities along four polarization directions, with the exposure time adjusted according to turbidity (ranging from 50 ms to 500 ms, with longer exposures used at higher turbidities) to avoid sensor saturation while maintaining adequate signal levels. From the recorded intensities, the Stokes vector was computed. Intensity images at arbitrary polarization angles were reconstructed from the Stokes vector, and the orthogonal pair yielding the highest contrast was selected and subtracted to produce the polarization-difference image.

Triangulation-based LiDAR employed the same underwater camera used for camera imaging, operating at a frame rate of 50 fps. The focused laser illumination beam remained stationary, while the target was translated continuously along an S-shaped trajectory using a motorized stage at a speed of approximately 15 mm/s. The laser spot position in each frame was extracted from the pixel coordinates, yielding an effective lateral sampling interval of approximately 0.3 mm. The camera-target axis and the laser beam formed an angle of approximately 30°. The surface depth (z-coordinate) was obtained by triangulating the laser spot position in each frame, with the x- and y-coordinates determined from the stage motion.

For quantitative comparison across different imaging modalities, structural edges were extracted from the images or rendered height maps and compared against a binary edge reference derived from the CAD model of the emblem. For LiDAR and LuDAR, the reconstructed point clouds were first rendered as frontal-view height-encoded maps. Prior to edge extraction, all edge-analysis inputs were converted to grayscale and smoothed using a Gaussian filter with σ = 2.0 pixels to suppress high-frequency noise. Edge maps were then generated using a Canny detector with adaptive thresholds determined from the Sobel gradient magnitude via Otsu thresholding. Specifically, the high threshold was selected automatically using Otsu's method, and the low threshold was set to 0.4 times the high threshold.

Precision and recall were evaluated using a pixel-wise edge-matching criterion by comparing the extracted edge maps with the CAD-derived binary edge reference. Two edge pixels were considered matched when their Euclidean distance was within a tolerance radius of 3 pixels. The corresponding F1-score was calculated as the harmonic mean of precision and recall:

$$F_1 = \frac{2PR}{P + R} \tag{2}$$

where P and R denote precision and recall, respectively.

Turbid-water experiments

All experiments were conducted in a water tank (40 × 40 × 100 cm^3). Turbid water was prepared using a fat emulsion (Intralipid, Yunbang), and the turbidity was monitored with a turbidimeter (SGZ-400B, Shanghai Yuefeng).

References

1. Liu, K., Ding, M., Pan, B. et al. A maneuverable underwater vehicle for near-seabed observation. Nat. Commun. 15, 10284 (2024).
2. Smith, C. R., Clark, M. R., Goetze, E. et al. Long-term impact and biological recovery in a deep-sea mining track. Nature 642, 112-118 (2025).
3. Onac, B. P., Polyak, V. J., Fornos, J. J. et al. Submerged bridge constructed at least 5600 years ago indicates early human arrival in Mallorca, Spain. Commun. Earth Environ. 5, 457 (2024).
4. Xu, S. et al. SonarSplat: Novel view synthesis of imaging sonar via Gaussian splatting. IEEE Robot. Autom. Lett. 10, 13312-13319 (2025).
5. Feng, Y. et al. Differentiable space carving for 3D reconstruction using imaging sonar. IEEE Robot. Autom. Lett. 9, 10065-10072 (2024).
6. Zhang, J. et al. A dense subframe-based SLAM framework with side-scan sonar. IEEE J. Ocean. Eng. 50, 1087-1102 (2025).
7. Sun, Z., Tian, T., Hu, H. et al. Extreme-depth water-related optical imaging:

conquering ultra-low illumination environments from epipelagic zone to Mariana Trench. PhotoniX 7, 7 (2026).

8. Ishimaru, A. Wave Propagation and Scattering in Random Media (Academic Press, 1978).
9. Thorstensen, J., Zonetti, S. & Thielemann, J. T. Light transport in turbid water for 3D underwater imaging. Opt. Express 32, 45013-45028 (2024).
10. Najar, U., Barolle, V., Balondrade, P. et al. Harnessing forward multiple scattering for optical imaging deep inside an opaque medium. Nat. Commun. 15, 7349 (2024).
11. Yoo, K. M. & Alfano, R. R. Time-resolved coherent and incoherent components of forward light scattering in random media. Opt. Lett. 15, 320-322 (1990).
12. Li, Y., Chen, Y., Zhang, J. et al. An underwater image restoration method with polarization imaging optimization model for poor visible conditions. IEEE Trans. Circuits Syst. Video Technol. 35, 3924-3939 (2025).
13. Amer, K. O. et al. Enhancing underwater optical imaging by using a low-pass polarization filter. Opt. Express 27, 621-643 (2019).
14. Su, Y., Zhang, Z., Lu, Y., Liu, S., Tang, Y. & Tian, J. Underwater descattering with polarization line constraint. Opt. Lasers Eng. 179, 108265 (2024).
15. Fang, M., Cai, Y. & Zhang, J. Image recovery method for underwater targets with complex polarization characteristics. Opt. Express 32, 19801-19813 (2024).
16. Li, Y., Zhang, J., Chen, Y. et al. Underwater image restoration via spatially adaptive polarization imaging and color correction. Knowl.-Based Syst. 305, 112651 (2024).
17. Wang, L. et al. Ballistic 2-D imaging through scattering walls using an ultrafast optical Kerr gate. Science 253, 769-771 (1991).
18. Wang, M., Wang, X., Zhang, Y. et al. Range-intensity-profile prior dehazing method for underwater range-gated imaging. Opt. Express 29, 7630-7640 (2021).
19. Jin, X., Du, D., Jin, J. & Fan, Y. Time-of-flight based imaging in strong scattering underwater environments. Opt. Express 32, 37247-37268 (2024).
20. Zhao, G., Ljungholm, M., Malmqvist, E. et al. Inelastic hyperspectral LiDAR for profiling aquatic ecosystems. Laser Photonics Rev. 10, 807-813 (2016).
21. Maccarone, A. et al. Submerged single-photon LiDAR imaging sensor used for real-time 3D scene reconstruction in scattering underwater environments. Opt. Express 31, 16690-16708 (2023).
22. Rehain, P. et al. Noise-tolerant single photon sensitive three-dimensional imager. Nat. Commun. 11, 921 (2020).
23. Li, H. et al. Noise-tolerant LiDAR approaching the standard quantum-limited precision. Light Sci. Appl. 14, 138 (2025).
24. Santos, J., Jakobsen, H. H., Petersen, P. M. et al. Remote 3D imaging and classification of pelagic microorganisms with a short-range multispectral confocal LiDAR. Laser Photonics Rev. 18, 2301291 (2024).

25. Liao, Z., Yang, Z., Shangguan, M. et al. Ranging accuracy improvement by using a spiral phase plate in a time-of-flight underwater lidar system. Opt. Laser Technol. 159, 109008 (2023).
26. Sørensen, F. F., Mai, C., Olsen, O. M. et al. Commercial optical and acoustic sensor performances under varying turbidity, illumination, and target distances. Sensors 23, 6575 (2023).
27. Zhao, F. et al. Metalens-assisted system for underwater imaging. Laser Photonics Rev. 15, 2100097 (2021).
28. Liang, H. et al. An optical meta-image-processor for enhanced imaging through strongly scattering media. Nat. Commun. 16, 9732 (2025).
29. Berman, D., Treibitz, T. & Avidan, S. Single image dehazing using haze-lines. IEEE Trans. Pattern Anal. Mach. Intell. 42, 720-734 (2020).
30. Fu, X. et al. A retinex-based enhancing approach for single underwater image. Proc. IEEE ICIP 4572-4576 (2014).
31. Liu, H. et al. Learning-based real-time imaging through dynamic scattering media. Light Sci. Appl. 13, 194 (2024).
32. Lyu, M. et al. Learning-based lensless imaging through optically thick scattering media. Adv. Photonics 1, 036002 (2019).
33. Zheng, S. et al. Incoherent imaging through highly nonstatic and optically thick turbid media based on neural network. Photonics Res. 9, B220-B228 (2021).
34. Shi, Y., Sheng, W., Fu, Y. et al. Overlapping speckle correlation algorithm for high-resolution imaging and tracking of objects in unknown scattering media. Nat. Commun. 14, 7742 (2023).
35. Yang, X., Liu, Y., Mou, X., Hu, T., Yuan, F. & Cheng, E. Imaging in turbid water based on a Hadamard single-pixel imaging system. Opt. Express 29, 12010-12023 (2021).
36. Park, J., Choi, S., Knieling, F. et al. Clinical translation of photoacoustic imaging. Nat. Rev. Bioeng. 3, 193-212 (2025).
37. Ha, M., Kim, J., Lee, J. et al. A handheld photoacoustic microscopic probe integrating a transparent ultrasound transducer and a fiber scanner. Nat. Commun. 17, 1409 (2026).
38. Na, S., Russin, J. J., Lin, L. et al. Massively parallel functional photoacoustic computed tomography of the human brain. Nat. Biomed. Eng. 6, 584-592 (2022).
39. Kang, S., Kwon, Y., Lee, H. et al. Tracing multiple scattering trajectories for deep optical imaging in scattering media. Nat. Commun. 14, 6871 (2023).
40. Stavn, R. H. Light attenuation in natural waters: Gershun's law, Lambert-Beer law, and the mean light path. Appl. Opt. 20, 2326-2327 (1981).
41. Li, B., Lin, Q. & Li, M. Frequency-angular resolving LiDAR using chip-scale acousto-optic beam steering. Nature 620, 316-322 (2023).
42. Juliano Martins, R., Marinov, E., Youssef, M. A. B. et al. Metasurface-enhanced light detection and ranging technology. Nat. Commun. 13, 5724 (2022).

43. Zhang, X., Kwon, K., Henriksson, J., Luo, J. & Wu, M. C. A large-scale microelectromechanical-systems-based silicon photonics LiDAR. Nature 603, 253-258 (2022).
44. Liang, D., Zhang, C., Zhang, P. et al. Evolution of laser technology for automotive LiDAR, an industrial viewpoint. Nat. Commun. 15, 7660 (2024).

Supplementary Files

This is a list of supplementary files associated with this preprint. Click to download.

- SupplementaryInformation.pdf